Taylor & Francis
Taylor & Francis Group

Science and Technology of Advanced Materials: Methods

ISSN: (Print) (Online) Journal homepage: https://www.tandfonline.com/loi/tstm20

Tensile deformation behavior of TRIP-aided bainitic ferrite steel in the post-necking strain region

Takashi Matsuno, Tomohiko Hojo, Ikumu Watanabe, Ayumi Shiro, Takahisa Shobu & Kentaro Kajiwara

To cite this article: Takashi Matsuno, Tomohiko Hojo, Ikumu Watanabe, Ayumi Shiro, Takahisa Shobu & Kentaro Kajiwara (2021) Tensile deformation behavior of TRIP-aided bainitic ferrite steel in the post-necking strain region, Science and Technology of Advanced Materials: Methods, 1:1, 56-74, DOI: 10.1080/27660400.2021.1922207

To link to this article: https://doi.org/10.1080/27660400.2021.1922207

Published online: 13 Jul 2021.

SCIENCE AND TECHNOLOGY OF ADVANCED MATERIALS: METHODS
2021, VOL. 1, NO. 1, 56–74
https://doi.org/10.1080/27660400.2021.1922207

Tensile deformation behavior of TRIP-aided bainitic ferrite steel in the post-necking strain region

Takashi Matsuno[a], Tomohiko Hojo[b], Ikumu Watanabe[c], Ayumi Shiro[d], Takahisa Shobu[e] and Kentaro Kajiwara[f]

[a]Engineering Faculty, Tottori University, Tottori, Japan; [b]Institute for Materials Research, Tohoku University, Sendai, Japan; [c]Research Center for Structural Materials, National Institute for Materials Science, Tsukuba, Japan; [d]Quantum Beam Science Research Directorate, National Institutes for Quantum and Radiological Science and Technology, Sayo-cho, Japan; [e]Nuclear Science Research Institute, Japan Atomic Energy Agency, Sayo-cho, Japan; [f]Industrial Application and Partnership Division, Japan Synchrotron Radiation Research Institute, Sayo-cho, Japan

ABSTRACT

Transformation induced plasticity (TRIP) steels present a remarkable balance of strength and ductility. However, their post-necking hardening behavior, which is required for press-forming and automobile crash simulation, is unreliable because of their stress-triaxiality dependency. Therefore, we analyzed the stress-triaxiality hardening in the post-necking strain regions of tensile loaded TRIP steel to accurately evaluate the stress and strain distribution. Tensile tests were accordingly conducted on small, round-bar specimens to evaluate the true stress vs. cross-sectional reduction ratio curves up to fracture. Additionally, the stress distribution inside each specimen was measured using synchrotron X-ray diffraction. Using these measurements, the hardening law for the TRIP steel was identified through a series of finite element (FE) simulations, in which a simplified phenomenological strain and stress-triaxiality hardening were found to agree well with the measurements in the post-necking strain region. As a result, the hardening rate of the TRIP steel showed a sudden decrease at the uniform elongation limit strain. The FE simulations including stress-triaxiality hardening successfully reproduced this hardening behavior up to the fracture, and the FE simulation including stress-triaxiality hardening and its saturation presented values closest to the XRD measurements. This simulation also agreed well with the measurements obtained in the tensile direction away from the neck center. A microstructural analysis of the retained austenite at the neck supported this result. The FE simulations revealed that a combination of the TRIP effect and its deactivation accelerates the localized deformation at the specimen neck under tensile loading.

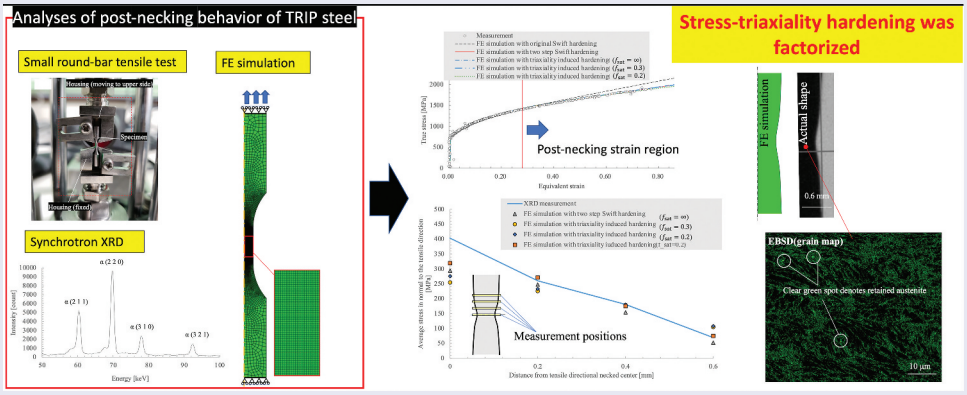

KEYWORDS

Advanced high-strength steel; large strain; stress-triaxiality; small round-bar tensile test; synchrotron X-ray diffraction; finite element simulation

CLASSIFICATIONS

Materials data generation

1. Introduction

Recently, advanced high-strength steels (AHSSs) have been developed that exhibit both high elongation and good tensile strength, thereby providing high impact energy absorption [1–3]. As a consequence of these favorable properties, AHSSs have been extensively used in automobiles. The substitution of thick mild steel sheets with thin AHSS sheets has resulted in a reduction in automobile weight without adversely affecting automobile crashworthiness.

In recent years, many researchers have analyzed the microstructures [4,5] and mechanical properties [6] of effective AHSSs to develop a new generation of AHSSs. As reviewed by Hance [7], current AHSSs can be classified into three generations according to the compatibility of strength and total elongation. Each generation is defined by its value of tensile strength multiplied by

CONTACT Takashi Matsuno matsu@tottori-u.ac.jp Tottori University, 4-101 Koyama-cho-minami, Tottori 680-8552, Japan

total elongation, and for the third generation, which is the most advanced at present, these values exceed 20GPa%. For the next generation of AHSSs, values exceeding 30GPa% are required.

Steels that present transformation induced plasticity (TRIP) effects are strong candidates for such next-generation AHSSs (hereafter referred to as TRIP steels). However, unpredictable post-necking deformation of TRIP steels presents difficulties for some automobile applications requiring preliminary numerical estimation of crashworthiness and press-formability. Such unpredictable deformation is caused by the sensitivity of stress-triaxiality to work-hardening (hereafter referred to as stress-triaxiality hardening), which is induced by the transformation of retained austenite with tensile deformation [8,9]. Indeed, many studies have determined that the hardening law for TRIP steels is a function of plastic strain and stress-triaxiality, and the numerical simulations with such hardening laws presented good agreement with the experiments [10–15].

To model post-necking work-hardening behavior, many researchers have attempted to extrapolate the flow stress using multiple strain hardening laws and validate their results using ductile fracture behavior [16,17], local strain distribution [18], and consistency with other types of mechanical tests [19,20]. However, such extrapolations cannot express the stress-triaxiality hardening of TRIP steels because the stress-triaxiality is constant before necking and only begins to increase in the post-necking strain region. Thus, instead of extrapolation, some studies have deduced the post-necking flow stress by analyzing the heterogeneous strain distribution in the neck using sheet metal tensile tests [21–23]; however, these methods also have excluded the stress-triaxiality hardening.

Evaluation of the actual stress-triaxiality is also associated with the analysis of post-necking deformation. Although finite element (FE) simulations employing strain hardening have demonstrated concurrence between the simulated strain distribution and the stress vs. strain curves obtained from actual measurements [18,24], these results have not been validated in terms of actual stress states. Notably, stress-triaxiality evaluation based on a strain hardening analysis may deviate the actual stress triaxiality inside necked TRIP steel specimens owing to the combination of stress-triaxiality hardening and heterogeneous plastic deformation for TRIP steels.

As the accurate prediction of the actual stress distribution in TRIP steel is essential for the improvement of crashworthy and press-formable automobile parts, in this study, the difficulties reviewed herein were overcome to reveal the role of stress-triaxiality hardening in the actual stress distribution within the necked region of an advanced TRIP steel. A dual-phase (DP) steel was also analyzed as a reference to serve as a validation of our methodology. To evaluate the work-hardening behavior in the post-necking strain region, small, round-bar tensile tests were conducted to measure the minimum diameter of the specimen during necking. The greater the strain experienced by a round-bar, the greater is its decrease in thickness; thus, the local strain can be approximated by the cross-sectional reduction ratio of a round-bar specimen in tensile tests, even at the neck [25,26]. An FE simulation was then applied to numerically replicate these tensile tests and obtain strain and stress-triaxiality hardening laws that concurred with the true stress vs. cross-sectional reduction ratio curves observed in the tests using the imposed force and minimum diameter. The stress and strain distributions inside the tensile specimen were also evaluated by these FE simulations. Furthermore, in-situ stress measurements were conducted inside the tensile specimens using synchrotron X-ray diffraction (XRD). These measurements were then compared to the FE simulations with and without considering stress-triaxiality effect on the work-hardening law, in which parameters were identified from the true stress vs. cross-sectional reduction ratio curves. Using this comparison, a simplified stress-triaxiality hardening law was developed that classifies the stress-triaxiality effect in terms of the post-necking hardening behaviour.

2. Materials and methods

2.1. Materials

The chemical compositions of the laboratory-made DP (DP590) and TRIP (TRIP980) steel sheets are shown in Table 1. Their thicknesses were 6.0 mm and 3.2 mm, respectively.

The DP steel sample was vacuum-melted in the laboratory. It was thinned to 6.0 mm by hot rolling above 1173 K, then air-cooled to 923 K, and finally water-quenched to room temperature (300 K). The TRIP sample was also vacuum-melted and forged to a thickness of 6.0 mm. Then, the slab was hot-rolled to 3.2 mm after annealing at 1473 K for 3600 s. This hot-rolled steel sheet was finally annealed at 1188 K for 1200 s followed by an austempering treatment at 698 K for 500 s.

The TRIP steel included an approximately 26% volumetric fraction of retained austenite, as determined using a commercial XRD analyzer. The matrix of the TRIP steel was composed of bainitic

Table 1. Chemical composition of the two steels (mass%).

	C	Si	Mn	S	Al	Nb	Mo
DP steel	0.049	0.49	1.99	0.0013	0.029	-	-
TRIP steel	0.40	0.49	1.48	0.0009	0.96	0.024	0.10

ferrite. Figure 1 presents the scanning electron microscope (SEM) image and inverse pole figure (IPF) of the retained austenite grains obtained by electron back scattering diffraction (EBSD). These images were obtained at the thick part of the small, round-bar tensile specimen detailed below in **Section 2.2**. This type of TRIP steel is called TRIP-aided bainitic ferrite steel, which demonstrates remarkable elongation [27] and fracture resistance [28].

The mechanical properties of the two types of steels were evaluated using the sheet specimen in the JIS-Z2241 specifications; their results are shown in Table 2. As evident, the DP and TRIP steels demonstrated tensile strengths of 590 and 980 MPa, respectively. The TRIP steel displayed remarkable uniform total elongation, presenting twice that of the DP steel and a significantly higher tensile strength. As the value of the tensile strength multiplied by the total elongation was 35GPa%, this TRIP steel can be considered a next generation AHSS, as discussed in **Section 1**.

2.2. Tensile tests for true stress–cross-sectional reduction ratio measurements using small, round-bar specimens

The small, round-bar specimen geometry shown in Figure 2 was used for the tensile tests. These round-bar specimens were cut from the center quarter-thickness of the steel sheets so that the tensile direction corresponds to the transverse direction of the material, where each specimen for tensile test and XRD measurement was located in the neighboring sites. The diameter of the central cross-section of each specimen was 1.0 mm, which enabled X-ray transmission into the specimen central axis. Both shoulders of the specimen increased in diameter to 2.5 mm. The length of the parallel section was designed to be 2.0 mm so that necking would occur at the center of the parallel section.

A custom-made, compact, tensile test machine (Miyakojima-seisakusyo Corporation Ltd., Japan)

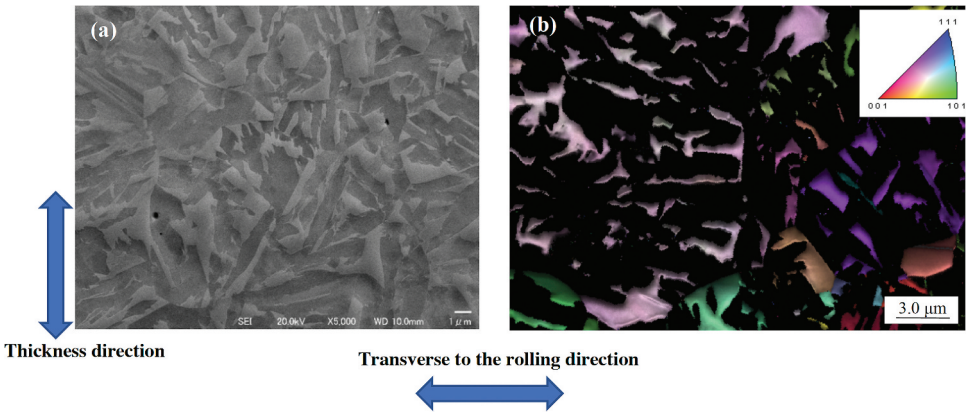

Figure 1. Microstructure of the TRIP steel used in this study. (a) SEM image. (b) IPF map of the austenite grains obtained by EBSD analysis with a 0.04 μm step, where the black areas are bainitic ferrite.

Table 2. Mechanical properties of the sheet-type, tensile specimens, evaluated by No. 5 specimen according to JIS Z2241 specifications.

	Yield stress [MPa]	Tensile strength [MPa]	Uniform elongation [%]	Total elongation [%]
DP steel	288	574	17.9	32.8
TRIP steel	738	1026	34.2	41.4

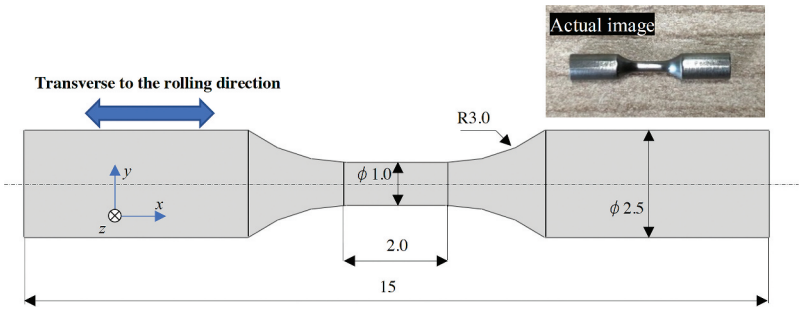

Figure 2. Small, round-bar specimen for tensile tests. Dimensions are in mm.

was used to apply tension to the test specimens at a head speed of approximately 2 μm/s. An external view of this machine is shown in Figure 3. Both shoulders of the specimens were fit into the specimen housings to apply tension (Figure 3(a)). The tensile force was measured by a load cell. To evaluate the strain, the change in the minimum diameter (D_m) of each specimen was measured via LED projection using a two-dimensional optical micrometer (TM006, Keyence Corporation, Japan). Figure 3(b) depicts the apparatus setup. The two-dimensional optical micrometer was used to measure the specimen shape in two directions; this measurement was conducted on only one side because the small, round-bar specimen maintained an almost constant circular cross-section during the tensile tests, as exemplified in Figure 4. Although rougher external shapes were observed for some specimens, the external lines of the fracture surfaces almost formed complete circular shapes, as shown in Figure 4. Indeed, the evaluations of each fracture surface roundness, calculated as $(D_{F,max} - D_{F,min})/2$, were 10.4 and 11.4 μm where $D_{F,max}$ and $D_{F,min}$ denotes maximum and minimum diameters, respectively, among 6 measurements with 30° pitches.

Instead of measuring the elongation, the cross-sectional reduction ratio, ρ, was obtained during these tensile tests. The value of ρ was defined as

$$\rho = 2\ln\left(\frac{D_{ini}}{D_m}\right) \quad (1)$$

where D_{ini} denotes the initial diameter, and D_m denotes the minimum diameter of the specimen. Assuming a constant volume, a complete circular cross-section, and a relatively minute elastic strain in the deformed part, ρ can be considered equal to the equivalent plastic strain $\bar{\varepsilon}_p$ [25]. The true stress in the specimen σ_t was calculated using the measured force F and the minimum diameter D_m as follows:

$$\sigma_t = \frac{4F}{\pi D_m^2}. \quad (2)$$

2.3. Synchrotron XRD measurements

2.3.1 Experimental setup

Synchrotron XRD measurements were performed at beamline BL28B2 of SPring-8, a large synchrotron radiation facility in Japan, whose bending magnet source can provide high-energy, white X-rays (having a wide range of photon energies). The specimens

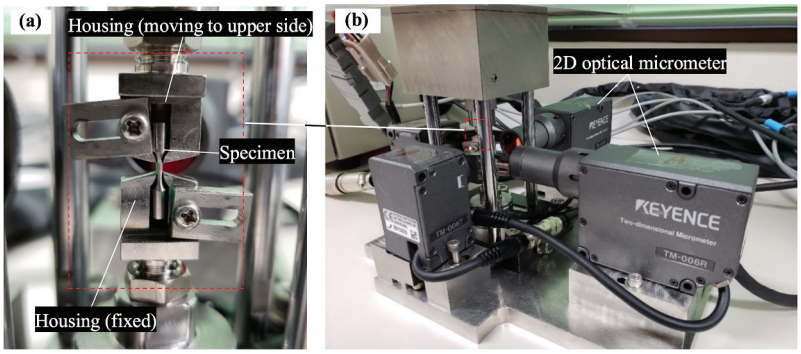

Figure 3. Tensile test machine for the small, round-bar specimens. (a) Magnified image of the specimen housing, and (b) external view of the compact tensile test machine.

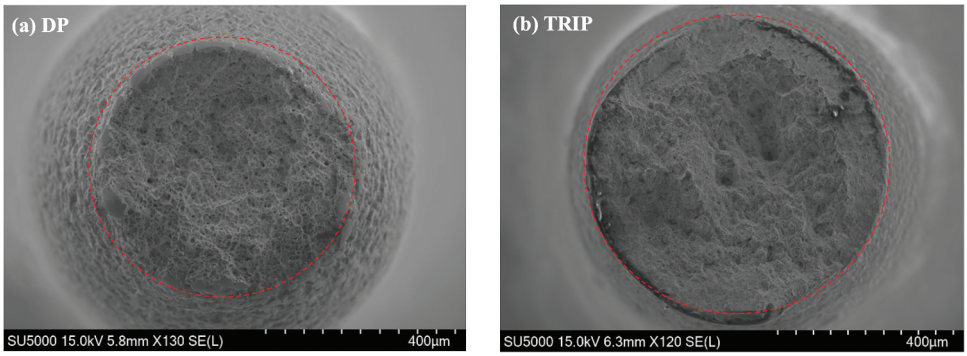

Figure 4. SEM images of the fractured specimen surfaces. Dotted lines present complete circular shapes surrounding the fracture surfaces.

shown in Figure 2 were tensioned on a small, hand-operated tensile machine positioned on the diffractometer. As a stepwise tensile load was applied, the XRD patterns of points located 0.0, 0.2, 0.4, and 0.6 mm from the x (tensile) directional center of the necked part were recorded in the x and z (normal-to-tensile) directions at each step. This process was repeated until the specimen fractured.

Figure 5 schematically illustrates the strain measurement process using synchrotron XRD. The transmission mode was used with a 5.0° diffraction angle. High-energy, white X-rays above 100 keV, which enabled transmission through a 1.0 mm diameter specimen, were programmed to emit in a 0.05 mm wide and 0.1 mm high beam by slit 1 and were collected by a solid-state detector (SSD, ORTEC GLP-16, 195/10P4, Seiko eg&g Corporation Ltd., Japan). To evaluate the local strain, slits 2 and 3 limited the area where the diffraction signal was measured, and their sizes are shown in Table 3.

As shown in Figure 6, the lengths of the rectangular gauge volumes were 0.05 mm in the measured lattice strain direction and 0.856 mm in a direction normal to the lattice strain direction. This high aspect quadrangle was approximated as an elongated rectangle. In the direction normal to the paper sheet in Figure 6, the gauge volume for the lattice strain measurements was an elongated quadrangle of 0.1 mm thickness.

Furthermore, after each step of the diffraction analysis, a radiographic image was recorded using monochromatic X-rays (60 keV) via a single silicon crystal, as shown in Figure 7. The minimum diameter of each small, round-bar specimen was determined from these radiographic images for obtaining the cross-sectional reduction ratio, ρ, using Equation (1).

2.3.2 Stress evaluation

The energy dispersion method [29] was used for the XRD measurements of the lattice strain. As exemplified in Figure 8, diffraction patterns of all the lattice planes were produced using white X-rays. Among these, the diffraction pattern of the α (3 2 1) plane at 92–93 keV was monitored because the Young's modulus for this lattice plane is close to the macroscopic Young's modulus. A Gaussian function was fitted to this diffraction pattern to derive the peak center by the minimum least

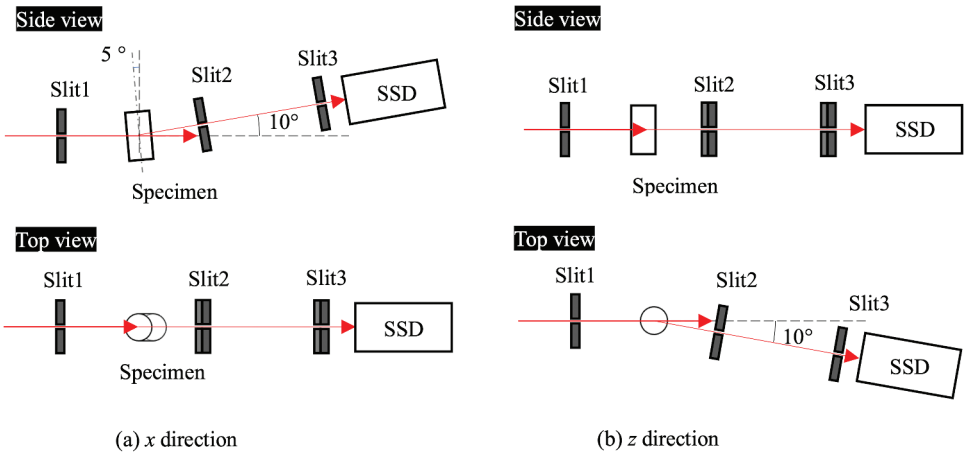

Figure 5. Schematic representation of the lattice strain measurement using the synchrotron XRD.

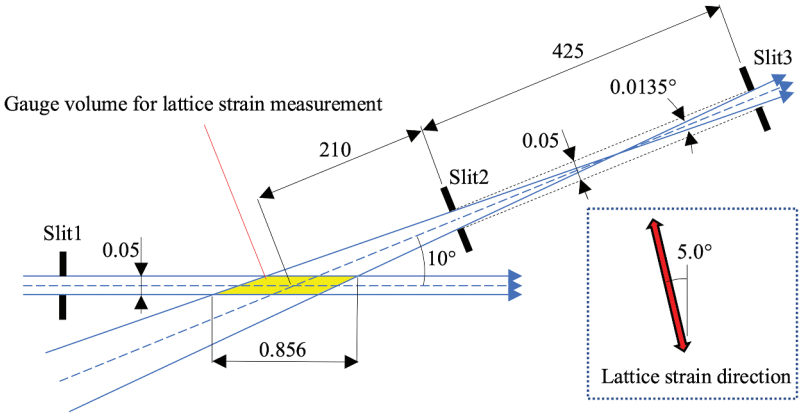

Figure 6. Schematic of the gauge volume for the lattice strain measurement. The lengths are reported in mm. Note this image is not to scale for readability.

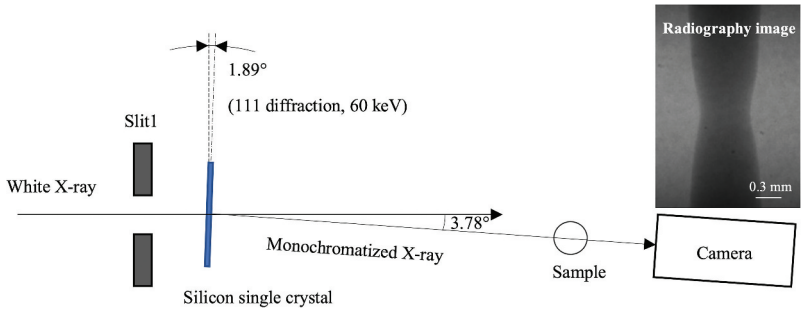

Figure 7. Schematic representation of the X-ray radiography process and example of an obtained radiographic image.

Table 3. Slit width for lattice strain measurement by XRD.

	Slit width for measuring the tensile directional lattice strain [mm]		Slit width for the measuring the lattice strain normal to the tensile direction [mm]	
	Tensile direction	Normal direction	Tensile direction	Normal direction
Slit 1	0.05	0.1	0.1	0.05
Slit 2	0.05	5.0	5.0	0.05
Slit 3	0.05	5.0	5.0	0.05

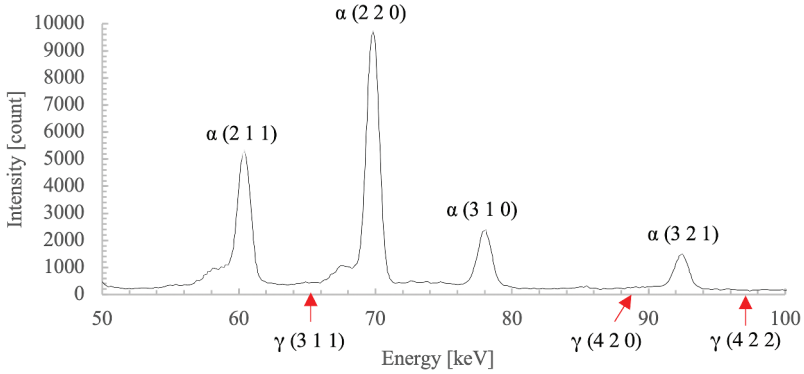

Figure 8. Diffraction pattern measurement of the TRIP steel at $\rho = 0.98$ (in the tensile direction).

square method, and its shift due to specimen deformation was translated to the lattice (elastic) strain by

$$\varepsilon = \frac{e_d - e_{ini}}{e_{ini}}, \tag{3}$$

where e_{ini} and e_d denote the pre- and post- deformation diffraction (energy dispersion) peak centers, respectively. Although the diffraction patterns from the three phases were detected in some cases during the measurements, we mainly focused on the patterns of the bainitic ferrite phase, which is the main constituent of this TRIP steel; the diffraction patterns of the other two phases were too weak to be used in evaluating the lattice strains. Therefore, the unsymmetric bottom parts of the diffraction patterns were cut to precisely fit the peak positions of the bainitic ferrite signals in the Gaussian fitting process. This was considered acceptable as fresh martensite, transformed from the austenite, caused the unsymmetric bottom parts.

To provide information consistent with previous studies of post-necking hardening behavior, we intended to present the stress distribution rather than the lattice strain. However, the calculation of stress requires the lattice strains in the x, y, and z directions. It was not possible to use XRD to measure the y-directional lattice strains in the same gauge volume used to measure the x- and z-directional lattice strains, because the X-rays would have to be injected from the top or bottom of the tensile specimen along the tensile direction. To solve this problem, we assumed that the averaged z-directional lattice strain was equal to the y-directional lattice strain. This assumption means that the gauge length in the y direction virtually increased and became equal to that in the z direction. Therefore, the abovementioned assumption does not affect the accuracy of stress evaluation. Under this assumption, the stresses were calculated as follows:

$$\sigma_{xx} = \frac{\hat{E}}{(1+\hat{\nu})(1-2\hat{\nu})}((1-\hat{\nu})\varepsilon_{xx} + 2\hat{\nu}\varepsilon_{zz}), \tag{4}$$

$$\sigma_{zz} = \frac{\hat{E}}{(1+\hat{\nu})(1-2\hat{\nu})}(\hat{\nu}\varepsilon_{xx} + \varepsilon_{zz}), \tag{5}$$

where σ_{xx} and σ_{zz} denote the stresses in the x and z directions, respectively; ε_{xx} and ε_{zz} denote the lattice strains calculated by Equation (3) in the x and z directions, respectively; and $\hat{E}$ and $\hat{\nu}$ denote the X-ray elastic constant and Poisson ratio, respectively, derived from mean field theory using the Kröner model [30], which has been widely used for this purpose in the literature [31]. The values of $\hat{E}$ and $\hat{\nu}$ for the α (3 2 1) plane were calculated to be 223.45 GPa and 0.2729, respectively.

Furthermore, the measurement errors of the stress, $\Delta\sigma$, were evaluated from the covariance between the measurement plots and fitted Gaussian curves as follows: The error values for the diffraction peak centers, Δe_d, were evaluated as the standard deviation calculated from the covariance, and the measurement errors for the lattice strain, $\Delta\varepsilon$, were evaluated using Equation (3) as $\Delta\varepsilon \approx \pm\Delta e_d / e_{ini}$. Then, $\Delta\sigma$ was evaluated by substitution of each directional component of $\Delta\varepsilon$ into Equations (4) and (5).

2.4. Finite element simulation

2.4.1 Meshes and boundary conditions

A commercial FE solver (Abaqus/Standard, Dassault Systèmes) was used for the simulations in this study with the static-implicit solver selected. As shown in Figure 9, the tensile specimen was meshed using axisymmetric, two-dimensional, quadrilateral elements with full integration, defined in Abaqus as 'CAX4.' The mesh size parallel to the specimen axis was 0.01 mm. To start the necking at the center, the diameter of the x-directional center was set 10^{-3} mm smaller than the rest of the parallel section. As also shown in Figure 9, one side of the specimen was constrained in the x direction, and a displacement of 0.8–1.0 mm was imposed on the other side. The resulting σ_t–ρ curves were evaluated in the same manner as in the actual tests. The x- and z- directional stresses used for comparison with the XRD measurements were evaluated as the element-area-averaged components in the gauge volume shown in Figure 9. Unloading simulations were also conducted so that the element-averaged x-directional stress in the FE simulation corresponded to the XRD-measured stress using Equation (4) during the stepwise tensile test, when the specimen was unavoidably unloaded because of mechanical gaps in the tensile machine and stress relaxation due to material viscosity [32].

2.4.2 Constitutive laws

The mechanical behaviors of the specimen materials were characterized in terms of their isotropic elasticity with a Young's modulus of 206 GPa, von Mises plasticity, associated flow rule, and isotropic hardening. The circular shapes of the fractured tensile specimens, shown in Figure 4, supported material isotropy, which caused the ellipsoidal shape of the fractured specimen surfaces [33]. Furthermore, rate-independent hardening was introduced because the rate dependency for this type of TRIP steel is sufficiently small within the strain rate of $2 \times 10^{-3} - 2 \times 10^{-2}$ used in this study [28]. The following flow stress, $Y(\bar{\varepsilon}_p, f)$, was used to explore the post-necking hardening behavior:

$$Y(\bar{\varepsilon}_p, f) = (1-a)Y_s(\bar{\varepsilon}_p) + a\{Y_l(\bar{\varepsilon}_p) + b\} + M_0 f, \tag{6}$$

where $\bar{\varepsilon}_p$ denotes the equivalent plastic strain, M_0 denotes the material constant for stress-triaxiality hardening, and f is the integration of the stress-triaxiality time derivative. The other parameters in Equation (6) are explained in the following paragraphs.

Except the term representing the stress-triaxiality hardening, $M_0 f$, Equation (6) represents a modified Swift law whose n value changes at a switching strain $\bar{\varepsilon}_{switch}$. The reason for applying this strain hardening law is the ease of parameter identification in the post-necking strain region. Other strain hardening laws for post-necking [26,34,35] can fit the FE simulation to the measured σ_t –ρ curves, but these fittings require more complicated procedures.

The function $Y_s(\bar{\varepsilon}_p)$ in Equation (6) denotes the equivalent stress, for which $\bar{\varepsilon}_p \leq \bar{\varepsilon}_{switch}$ is calculated by the original Swift hardening law [36] as follows:

$$Y_s(\bar{\varepsilon}_p) = K_1(\bar{\varepsilon}_p + c_1)^{n_1}, \tag{7}$$

where K_1, c_1, and n_1 are material constants. The next function, $Y_l(\bar{\varepsilon}_p)$, denotes the equivalent stress where $\bar{\varepsilon}_p > \bar{\varepsilon}_{switch}$ and is also calculated by the original Swift

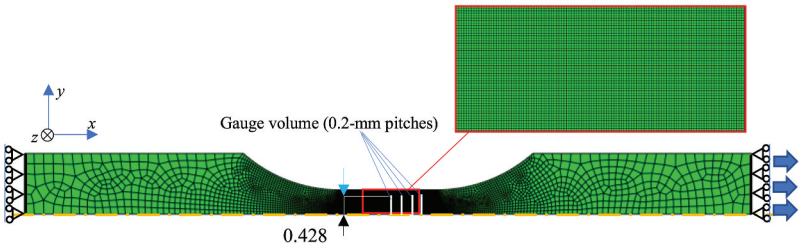

Figure 9. Finite element model for the tensile simulations.

hardening law, but with different material constants as follows:

$$Y_l(\bar{\varepsilon}_p) = K_2(\bar{\varepsilon}_p + c_2)^{n_2}, \tag{8}$$

The two curves are smoothly connected at $\bar{\varepsilon}_p = \bar{\varepsilon}_{switch}$ by defining a and b in Equation (6) as follows:

$$a = \frac{\tanh\left(R(\bar{\varepsilon}_p - \bar{\varepsilon}_{switch})\right) + 1}{2}, \tag{9}$$

$$b = Y_l(\bar{\varepsilon}_{switch}) - Y_s(\bar{\varepsilon}_{switch}), \tag{10}$$

where R was set to 50 in this study.

Given the accuracy of the uniform elongation strain, tensile strength, and initial yield stress obtained in the FE analysis, K_i and c_i for $i = 1, 2$ in Equations (7) and (8) were derived using the following nonlinear simultaneous equations based on plastic instability analysis, rather than curve-fitting with the least-squares method:

$$K_i = \frac{Y_0}{c_i^{n_i}}, \tag{11}$$

$$c_i = \left(\frac{n_i^{n_i} Y_0}{\exp(\bar{\varepsilon}_u) T_s}\right)^{\frac{1}{n_i}}, \tag{12}$$

where Y_0 denotes the initial yield stress, T_s denotes the tensile strength, and $\bar{\varepsilon}_u$ denotes the true strain at the maximum nominal stress. These parameters were obtained from the tensile tests in this study; the parameters obtained from the sheet-type specimen (shown in Table 2) were not used. The n value for $Y_s(\bar{\varepsilon}_p)$, i.e. n_1, was also derived based on the plastic instability analysis as follows:

$$n_1 = c_1 + \bar{\varepsilon}_u. \tag{13}$$

Since $c_1 \ll \bar{\varepsilon}_u$, Equation (13) can be approximated as:

$$n_1 \approx \bar{\varepsilon}_u, \tag{14}$$

which was substituted into Equations (11) and (12) to derive K_1 and c_1.

The variable $\bar{\varepsilon}_{switch}$ was easily identified by comparing the measured and simulated σ_t–ρ curves using the original Swift hardening law. These two curves corresponded to each other until a particular strain was reached; this strain was identified as $\bar{\varepsilon}_{switch}$ assuming that $\rho \approx \bar{\varepsilon}_p$. The value of n_2 was fitted so that the measurements and the FE simulations agreed over the entire σ_t–ρ curve. In this study, the trial value of n_2 was gradually decreased from $n_2 = n_1$ until the FE simulation presented the closest agreement with the measurements. Note that K_2 and c_2 are also fitting parameters, but they were derived by substituting n_2 into Equations (11) and (12) for simplicity.

The term $M_0 f$ was introduced to describe the stress-triaxiality hardening caused by stress-triaxiality-induced austenite transformation into hard martensite in the post-necking strain region. Therefore, M_0 was set to zero for the DP steel. Although it represents a boldly simplified expression of stress-triaxiality hardening, this term is key in this study because it possibly expresses the particular stress and strain distribution inside the necked part of TRIP steel. The variable f, which is initially zero, is used to express the stress-triaxiality history imposed on the tensile specimen, and is defined as:

$$\dot{f} = \dot{\eta}. \tag{15}$$

For > 0, $\bar{\varepsilon}_p > \bar{\varepsilon}_u$, and $f < f_{sat}$, where η denotes the stress triaxiality $(\sigma_{xx} + \sigma_{yy} + \sigma_{zz})/3\bar{\sigma}$, in which $\bar{\sigma}$ is the equivalent stress and t_f denotes the time at which the deformation ceased. For the else conditions, $\dot{f}$ is set to be zero. Without these inequality conditions, the value of f would correspond to the stress-triaxiality increment from the uniaxial state. To focus on the post-necking behavior, the condition $\bar{\varepsilon}_p > \bar{\varepsilon}_u$ imposes $f = 0$ during uniform deformation, and therefore f begins to increase only after necking. The condition $f < f_{sat}$ imposes stress-triaxiality hardening saturation due to the saturation of the austenite transformation. When f reaches f_{sat}, the increase in the f value stops. The material constant M_0 was multiplied by this value of f and added onto the flow stress calculated by the strain hardening terms in Equation (6).

Note that Equation (15) was developed from the constitutive law of austenite transformation into martensite proposed by Stringfellow et al. [10]. In this constitutive law, the time derivative of martensite $\dot{v}_m$ transformed from the retained austenite can be expressed as follows:

$$\dot{v}_m = (1 - v_m)(A_f \bar{\varepsilon}_p + B_f \dot{\eta}) \tag{16}$$

where A_f and B_f are the functions of equivalent plastic strain and stress triaxiality, respectively. The volumetric fractions of retained austenite, martensite, and the other phases calculated by the transformation law can be used to obtain the TRIP steel flow stress using an averaging law [12]. This rigorous model presented good agreement with the measured σ_t–ρ curve and observed specimen neck geometry, but required too many material parameters to be identified from the σ_t–ρ curves of the tensile test. Thus, we propose the drastically simplified hardening law in Equation (6) because the hardening rates of retained austenite and martensite were saturated in the post-necking strain region, and the retained austenite fraction decreased quasi-linearly in the large strain region during the tensile test [37,38]. Furthermore, the Swift hardening law successfully expressed the stress–strain curve of TRIP steel only up to the uniform elongation limit [18]. This indicates that the effects of retained austenite transformation due

to increased plastic strain ($A_f \bar{\varepsilon}_p$ in Equation (16)) were included in the strain hardening terms in Equation (6). Consequently, it was assumed that the addition of the linear stress-triaxiality hardening term, $M_0 f$, could effectively express the hardening behavior in the post-necking strain region of the TRIP steel.

The fitted parameters in Equation (6) are shown in Table 4 (DP) and Table 5 (TRIP). Many parametric combinations were fitted for each material. In the case of $M_0 \neq 0$ for the TRIP steel, a small value of n_2 (0.02) was used because the effect of the stress-triaxiality hardening on the stress distribution inside the specimen became clear. In this case, M_0 was fitted by trial and error using FE simulations in which $f_{sat} = \infty$ by gradually increasing M_0 until the simulated σ_t–ρ curve agreed with the measurements. After this, the other two cases with $f_{sat} = 0.3$ and 0.2 were evaluated. These f_{sat} values were heuristically set so that their evident influence on the stress distribution was manifested without influencing the σ_t–ρ curves too much.

Table 4. Hardening parameters of the DP steel fitted from the small, round-bar tensile tests. M_0 is set to zero.

	Y_0 [MPa]	T_s [MPa]	n_1	n_2	$\bar{\varepsilon}_{switch}$
Case 1	300	610	0.15		
Case 2	300	610	0.15	0.13	0.45

Table 5. Hardening parameters of the TRIP steel in Equation (6) fitted from the small, round-bar tensile tests.

	Y_0 [MPa]	T_s [MPa]	n_1	n_2	$\bar{\varepsilon}_{switch}$	M_0 [MPa]	f_{sat}
Case 3	730	1050	0.28				
Case 4	730	1050	0.28	0.17	0.28	0.0	
Case 5	730	1050	0.28	0.02	0.28	1310	∞
Case 6	730	1050	0.28	0.02	0.28	1310	0.3
Case 7	730	1050	0.28	0.02	0.28	1310	0.2

The hardening law presented in Equations (6)–(15) was implemented with the assumption of small deformations using the Abaqus user-defined material subroutine (UMAT). The updated Lagrangian method included in Abaqus was used to express large deformations. To avoid convergency problems, f was integrated by an explicit method, as reported in [13]. The value of f was maintained constant for each increment and was updated using Equation (15) at the next calculation step. Alternatively, a large number of calculation steps (200) was specified in the tensile loading step.

3. Results

3.1 Tensile test for true stress vs. cross-sectional reduction ratio curves

3.1.1 DP steel

Figure 10 depicts the σ_t–ρ curves of the DP steel, including both the measurements and FE simulations. The measurements recorded a maximum ρ of 1.1, which was clearly involved in the post-necking strain region. From Figure 10, both the FE simulations using the original (Case 1) and modified Swift (Case 2) hardening laws agreed well with the measurements. Case 1 deviated slightly from the measured values by exceeding the ρ of 0.45, which corresponded to the switching strain, and this slight deviation was corrected in Case 2.

Figure 11 presents the FE-simulated and observed neck geometries of the DP steel at $\rho = 1.0$. The FE simulations in both Cases 1 (Figure 11(a)) and 2 (Figure 11(b)) agreed well with the observations (Figure 11(c)) where the maximum error was approximately 0.03 mm in the radial direction, as seen at the bottom of the specimen figures (the FE simulations

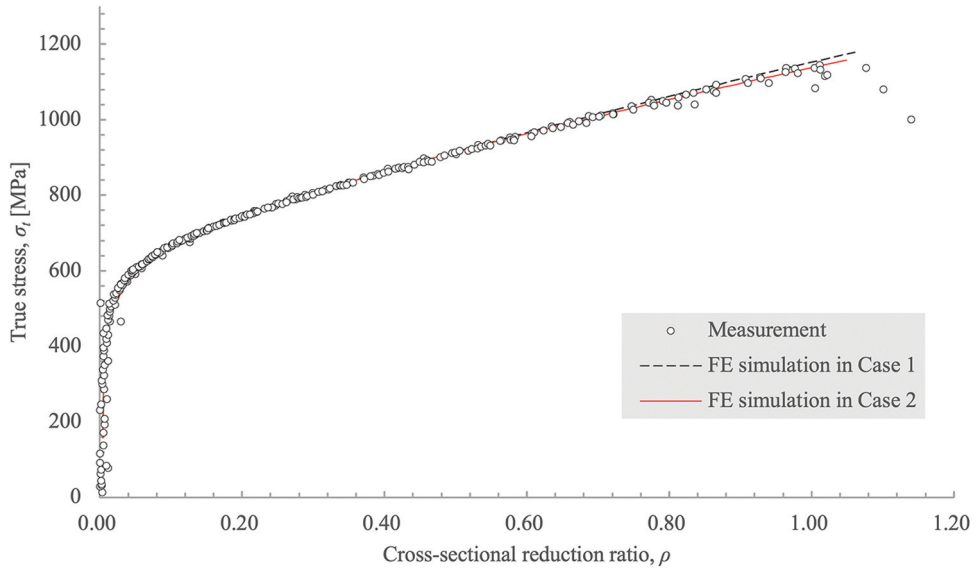

Figure 10. Measured and simulated σ_t –ρ curves of the DP steel.

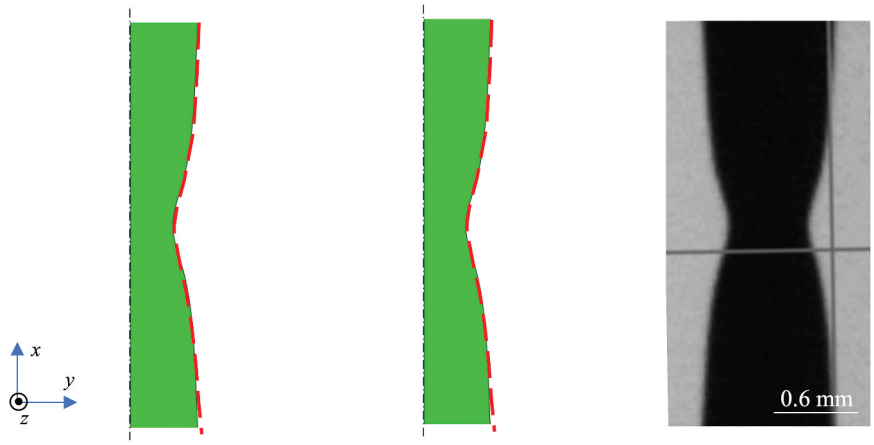

(a) FE simulation in case 1 **(b)** FE simulation in case 2 **(c)** Shape projection in the tensile test

Figure 11. Geometries of the specimens in the tensile tests using DP steel. The cross-sectional reduction ratio, ρ, was 1.0. (a) and (b) show the FE simulations with different hardening laws, where the red-dotted lines indicate the actual geometry obtained from the observation in (c) by the 2D optical micrometer.

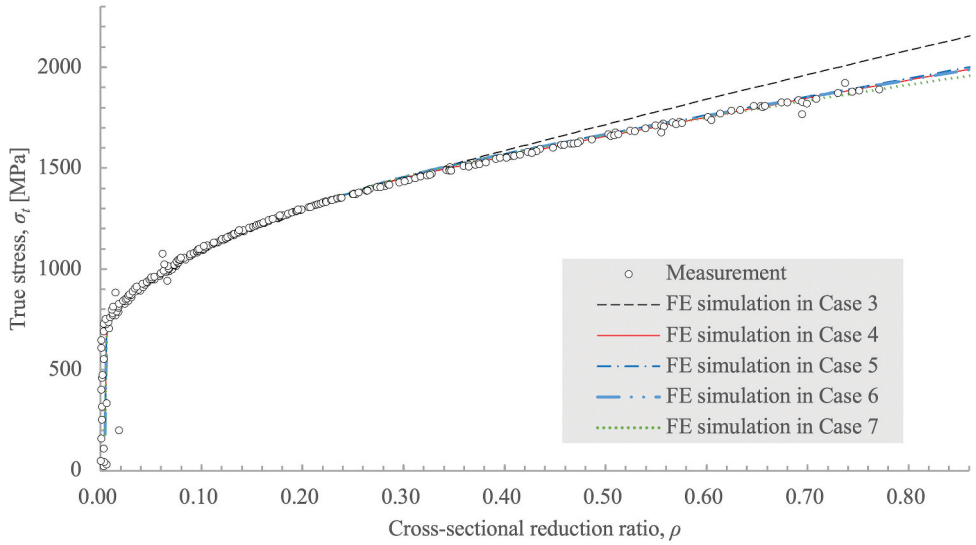

Figure 12. Measured and simulated σ_t –ρ curves of the TRIP steel.

present thinner radius than that of the observation). It is widely known that this sharp necking shape causes a higher σ_t because of a higher hydrostatic stress. Thus, the observed agreement in the neck geometry confirmed the accuracy of the hardening law parameters used in the FE simulations.

3.1.2 TRIP steel

Figure 12 presents the σ_t–ρ curves for the TRIP steel, in which the measurements as well as the results of five FE simulations (Cases 3 to 7) are included. Measurements were performed up to a maximum ρ of 0.77, where σ_t reached 1890 MPa. The values of Y_0, T_s, and n_1, shown in Table 5, evaluated using the small, round-bar specimen, were approximately equal to those evaluated using the sheet-type specimen in Table 2.

Except Case 3 (the original Swift hardening law), the FE simulations exhibited good agreement with the measurements over the entire σ_t–ρ curve. The σ_t–ρ curves in Cases 5–7 were approximately equal and overlapped in the figure. The smaller f_{sat} in Cases 6 and 7 decreased the σ_t around the maximum ρ, but this decrease was very small. It is notable that the original Swift hardening law in Case 3 resulted in a large deviation from the measurements. This deviation began to increase at $\rho = 0.28$, which approximated the $\bar{\varepsilon}_p$ where the necking occurred and was set as $\bar{\varepsilon}_{switch}$, as shown in Table 5. These tendencies were notably different from those of DP steel.

The neck geometries from the FE simulations were compared with the experimental observations and are shown in Figure 13. The simulations using each hardening laws (Figure 13(a–d)) resulted in the same neck

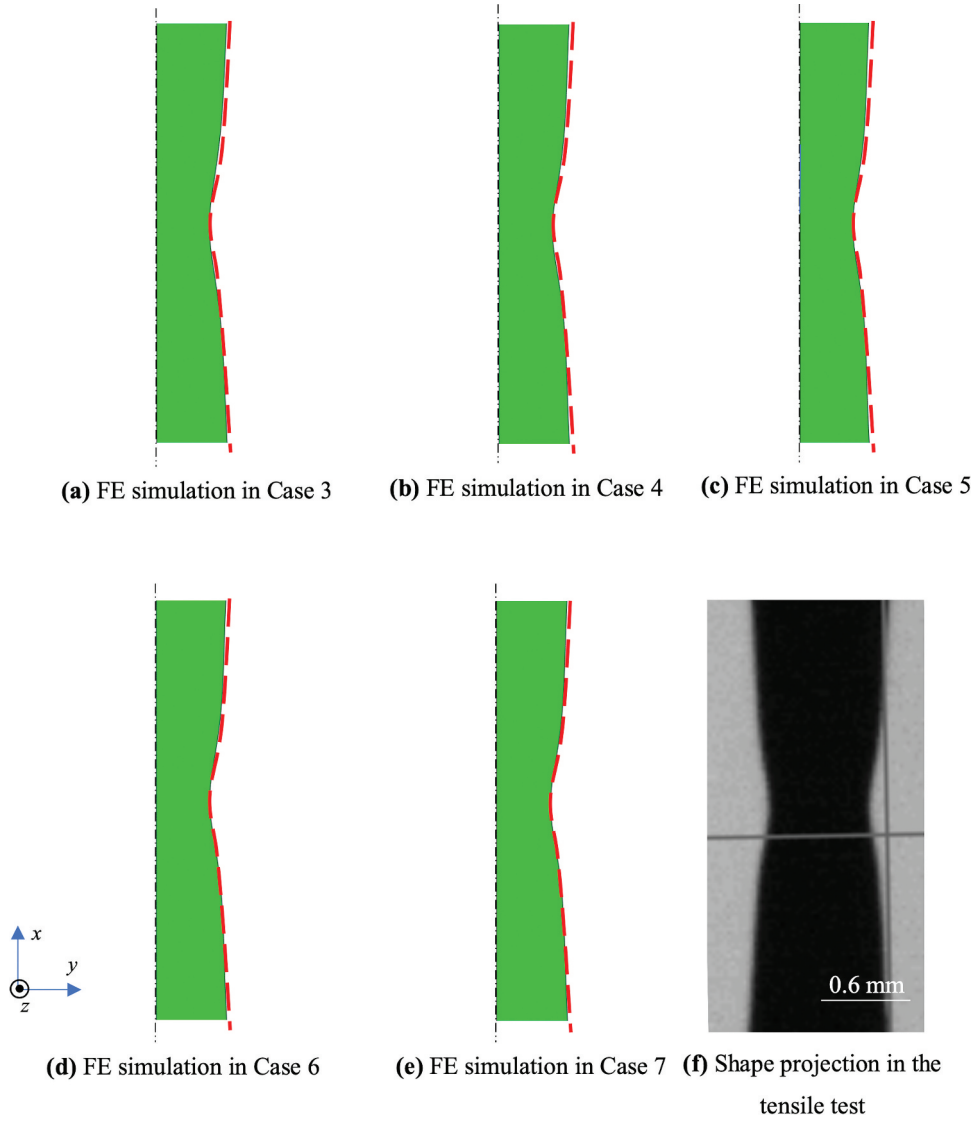

(a) FE simulation in Case 3 **(b)** FE simulation in Case 4 **(c)** FE simulation in Case 5

(d) FE simulation in Case 6 **(e)** FE simulation in Case 7 **(f)** Shape projection in the tensile test

Figure 13. Geometries of the specimens in the tensile tests using the TRIP steel. The cross-sectional reduction ratio, ρ, was 0.72. (a–e) show the FE simulations with different hardening laws, where the red-dotted lines indicate the actual, observed geometry in (f) obtained by the 2D optical micrometer.

geometry, which agreed well with the observations (Figure 13(f)). Actually, the neck geometry in the FE simulations overlapped the observation around the specimen axial center, and they presented smaller radius than the observation away from the center, where the maximum error in the radial direction was 0.025 mm, as seen at the top of figure. Combined with the good agreement of their σ_t–ρ curves, the FE simulations using the multiple hardening laws in Cases 4–7 successfully expressed the actual tensile behavior of the TRIP steel.

3.2 XRD measurements

3.2.1 DP steel

A remarkable tendency of the XRD measurements was observed alongside the change in the spatial gradient of σ_{xx}, in which the gradient increased as ρ increased. At $\rho = 0.33$ (Figure 14(a)), the spatial distribution of the XRD measurements did not exhibit a direct correlation with d, and the stress fluctuated within 400–600 MPa. At $\rho = 0.59$, the XRD measurements also displayed fluctuations, but the value at the most distant position ($d = 0.6$) was clearly smaller than those at the other three positions. The spatial gradient of the XRD measurements became clear at $\rho = 0.98$ and 1.01 (Figure 14(c and d)). Both of these cases presented stresses of approximately 920 MPa at $d = 0.0$ that monotonically decreased with increasing d. While the stresses at $d = 0.0$ were approximately equal in both cases, the gradient of the XRD measurement at $\rho = 1.01$ and 1305 MPa/mm, was higher than that at $\rho = 0.98$ and 1240 MPa/mm.

Aside from the measurement fluctuations, the numerically simulated spatial distribution of σ_{xx} was similar to the spatial distribution of the XRD measurements. The FE simulations resulted in an approximately flat stress distribution with respect to d at $\rho = 0.33$ (Figure 14(a)), a small, negative gradient

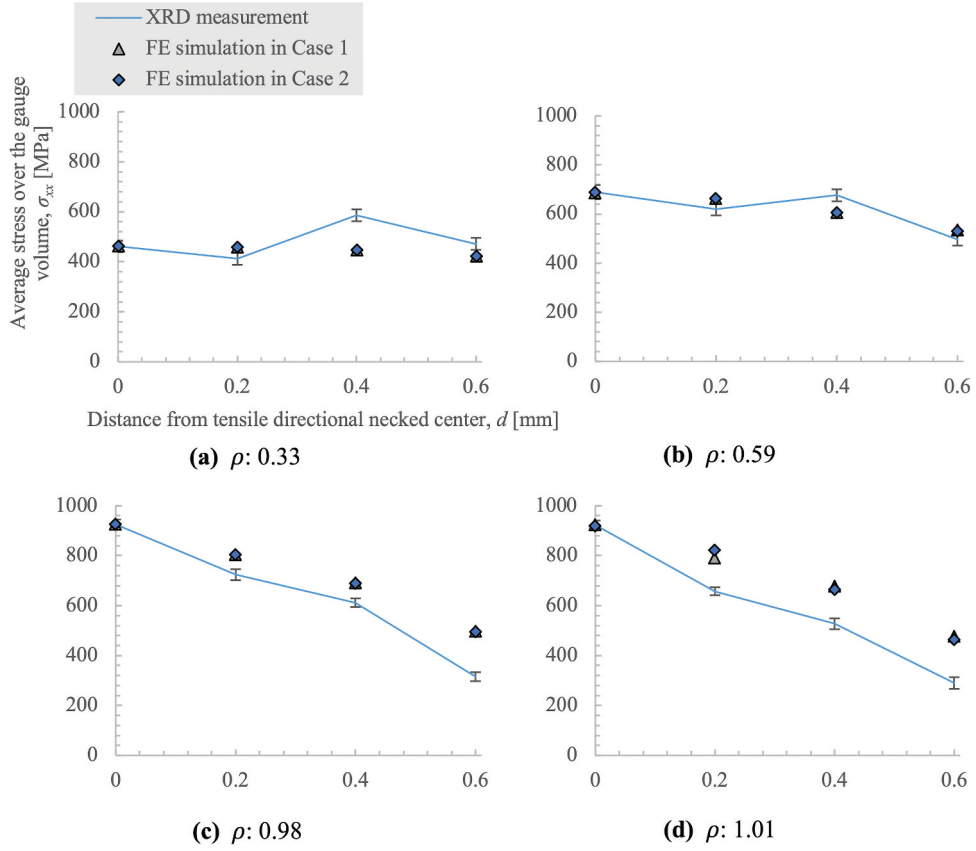

Figure 14. Comparison of the measured and FE-simulated *x*-directional stress averaged over the gauge volume of the DP steel. (a–d) show the comparison at different ρ levels. The FE simulations include an unloading step so that the *x*-directional stresses at the necking center agreed with the XRD measurements.

from $d = 0.0$ to 0.6 at $\rho = 0.59$ (Figure 14(b)), and high, negative gradients at $\rho = 0.98$and 1.01 (Figure 14(c and d)). The difference between the σ_{xx} values of Cases 1 and 2 was very small. It should be noted that the simulated gradient of σ_{xx} at $\rho = 1.01$ was smaller than that at $\rho = 0.98$, whereas the XRD measurements demonstrated the opposite behavior.

The behavior of the *z*-directional stress, σ_{zz}, was the same as that of σ_{xx}. Figure 15 depicts the fluctuating stress distribution at $\rho = 0.33$ (Figure 15(a)), a lower stress at $d = 0.6$ and $\rho = 0.59$ (Figure 15(b)), and a monotonic decrease from $d = 0.0$ to 0.6 at $\rho = 0.98$ and 1.01, as observed from the XRD measurements. Note that the distributions at $\rho = 0.98$ and 1.01 were approximately equal. At $d = 0.4$, the difference between the σ_{zz} values for $\rho = 0.98$ and 1.01 was 35 MPa, which was the largest observed in these tests. The other d values exhibited small differences of approximately 10 MPa.

It can be observed in Figure 15 that the FE simulations presented 40–50 MPa higher values of σ_{zz} at $d = 0.0$ for all ρ levels. For example, at $\rho = 0.98$ and 1.01, the FE simulations were higher at all the positions presented, though the curve shape was similar to that obtained from the XRD measurements.

3.2.2 TRIP steel

Figure 16 depicts the XRD measurements of the tensile directional stress, σ_{xx}, and the corresponding element-averaged stress in the FE simulations. The values of σ_{xx} for the TRIP steel tensile test were similar to those of the DP steel at $\rho = 0.98$ and 1.01. The XRD measurements monotonically decreased from $d = 0.0$ to 0.6. The spatial gradients corresponding to this stress decrease increased with increasing strain.

From Figure 16, most of the element-averaged stresses can be observed to display higher values of σ_{xx} compared with the XRD measurements. Among the FE simulation Cases 4–7, the simulated values were approximately equal, but at $\rho = 0.86$, each case showed deviations at $d = 0.4$ and 0.6, where Case 7 ($f_{sat} = 0.2$)exhibited the smallest values. All cases presented a monotonic decrease in their σ_{xx} gradients from $d = 0.0$ to 0.6, but these gradients were smaller than those obtained by the XRD measurements. In particular, the σ_{xx} gradients were remarkably small in the FE simulations between $d = 0.0$ and 0.2 at $\rho = 0.74$ and0.81.

In terms of the *z*-directional stress σ_{zz}, the XRD measurements also displayed a monotonic decrease with increasing d at all ρ levels (Figure 17). The gradient of σ_{zz} vs. d increased with increasing ρ. It is notable that the gradients between $d = 0.0$ and 0.2 were larger than those of the rest of the σ_{zz} vs. d curves. That is, the σ_{zz} measurement at $d = 0.0$ was significantly higher than those at other distances.

In contrast to the σ_{xx} results, most of the FE simulations predicted lower values of σ_{zz} that those

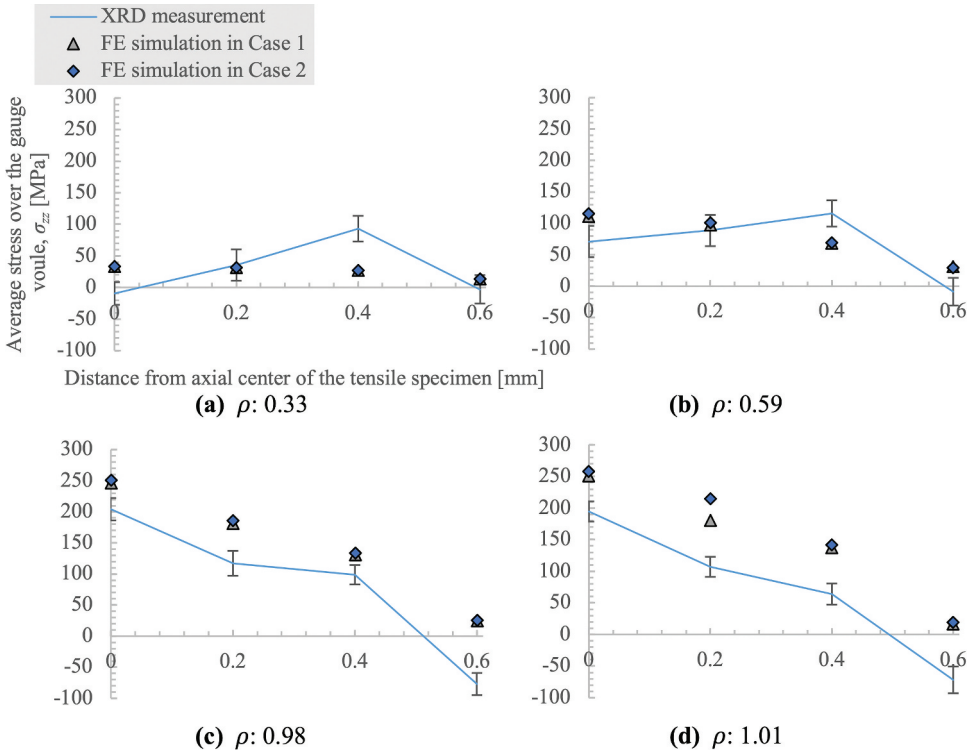

Figure 15. Comparison of measured and FE-simulated *z*-directional stress averaged over the gauge volume of the DP steel. (a–d) display the comparison at different ρ levels. The FE simulations include an unloading step so that the *x*-directional stresses at the center agree with the XRD measurements.

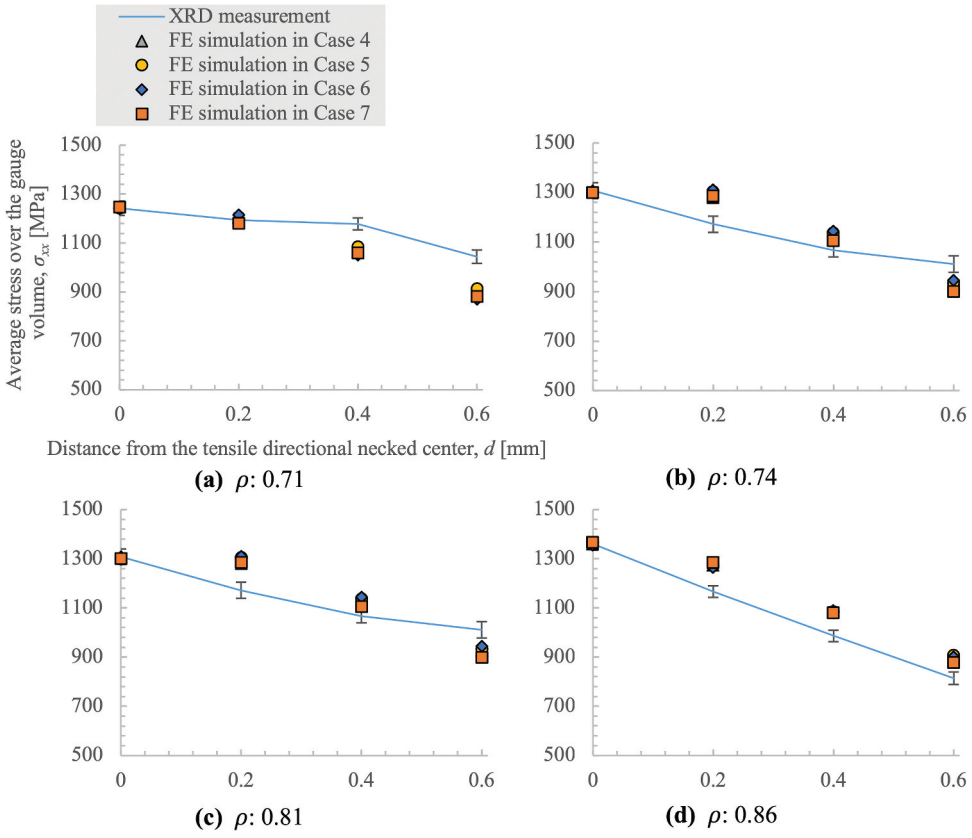

Figure 16. Comparison of the measured and FE-simulated *x*-directional stress averaged over the gauge volume of the TRIP steel. (a–d) display the comparisons at different ρ levels. The FE simulations include an unloading step so that the *x*-directional stresses at the neck center agree with the XRD measurements.

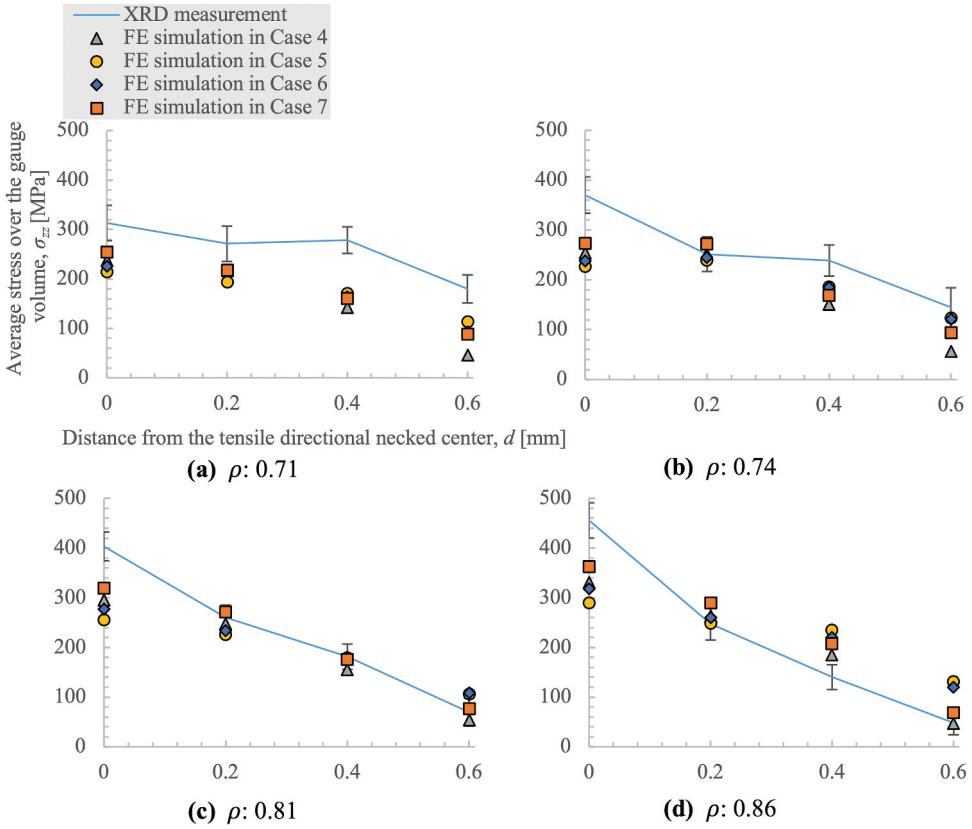

Figure 17. Comparison of the measured and FE-simulated *z*-directional stress averaged over the gauge volume of the TRIP steel. (a–d) display the comparisons at different ρ levels. The FE simulations include an unloading step so that the *x*-directional stresses at the neck center agree with the XRD measurements.

obtained by the XRD measurements, and the different hardening laws demonstrated different σ_{zz} trends (see Figure 17). Case 7 ($f_{sat} = 0.2$) showed the highest σ_{zz} at $d = 0.0$ for all ρ levels, while Case 5 ($f_{sat} = \infty$) showed the lowest σ_{zz}. Case 4 ($M_0 = 0$) and Case 6 ($f_{sat} = 0.3$) resulted in intermediate values of σ_{zz} that were approximately equal at $d = 0.0$ for all ρ levels. However, the values of σ_{zz} in Case 4 were smaller than those in the other cases at $d = 0.4$ and 0.6, where the largest difference was approximately 70 MPa at $d = 0.6$ for $\rho = 0.86$.

4. Discussion

4.1 True stress vs. cross-sectional reduction ratio curve

For both steels evaluated in this study, despite the small size of the tensile specimen, the measured tensile strength, yield stress, and uniform elongation (*n* value) reported in Tables 4 and Table 5 were close to those of the sheet specimen in the JIS-Z2241 evaluation shown in Table 2. Thus, we can consider the successful evaluation of σ_t–ρ curves.

In contrast to the DP steel, the FE simulation of TRIP steel using the original Swift hardening law disagreed with the measured σ_t–ρ curve in the post-necking strain region. The simulated σ_t–ρ curve deviated positively from the true measurements after necking occurred in the specimen. Therefore, the switching of the hardening law is mandatory to accurately express the post-necking σ_t–ρ curve. Thus, the method employed in this study combining the σ_t–ρ measurements and FE simulation with the simplified stress-triaxiality hardening law in Equation (6) has newly revealed this post-necking behavior.

It is interesting that the value of $\bar{\varepsilon}_{switch}$ corresponded to the value of $\bar{\varepsilon}_u$. A strong TRIP effect (the transformation of retained austenite into hard martensite with material deformation) is suggested by this result, in which the weakening of the TRIP effect caused the sudden switch of the *n* value at $\bar{\varepsilon}_u$. Evidently, the TRIP weakening effect on the *n* value is larger than that of the stress-triaxiality hardening because the latter would cause the *n* value to increase. However, the TRIP effect did not completely cease in the post-necking strain region as indicated by the high *n* value (n_2 = 0.17 in Case 4).

4.2 XRD measurements

A comparison between the XRD measurements and the FE simulations of the TRIP steel under tension validated the stress-triaxiality hardening behavior in the post-necking strain region. Although the FE simulations provided a positive bias for the stress evaluations compared with the XRD measurements for the

DP steel, they yielded a negative evaluation bias for σ_{zz}, normal to the tensile direction for the TRIP steel. Therefore, the TRIP effect positively shifted the σ_{zz} compared with the FE simulations, especially at $d = 0.0$. It is notable that Case 7 ($f_{sat} = 0.2$) presented the closest σ_{zz} at $d = 0.0$ for all evaluated ρ levels, as shown in Figure 17. The higher XRD measurement of σ_{zz} suggests a very small n_2 in the deactivation cases for the TRIP effect. Although setting $n_2 < 0.02$ presents a difficult convergence problem for the static-implicit FE method, the actual n_2 was indeed less than 0.02.

The positively biased σ_{zz} at $d = 0.6$ also suggests the validity of stress-triaxiality hardening in the post-necking strain region. Case 4 ($M_0 = 0$) resulted in the second highest σ_{zz} at $d = 0.0$, but the σ_{zz} values at $d = 0.6$ for ρ of 0.71 and 0.74 were lower than those observed for the other stress-triaxiality hardening cases. The XRD measurements of the DP steel displayed a significant decrease in σ_{zz} at $d = 0.6$ for $\rho =$ 0.98 and 1.01, but the XRD measurements of the TRIP steel showed a lower-gradient of σ_{zz} decrease at $d =$ 0.6 for all ρ values. The σ_{zz} distribution in the radial direction at $d = 0.6$ verified this low-gradient decrease, as shown in Figure 17. For the stress-triaxiality hardening laws in Cases 5–7, σ_{zz} at the specimen surface at $d = 0.6$ presented higher tensile values than for those in Case 4, regardless of the value of f_{sat}. This tendency could not be simulated without a positive deviation of the σ_t–ρ curve. Thus, stress-triaxiality hardening was mandatory for the accurate simulation of the σ_{zz} distribution.

In addition, note that the effect of stress relaxation was insignificant. This phenomenon must therefore dilute the initial stress distribution, but the XRD measurements present a steeper distribution than the FE simulations. Thus, the above analysis was not negated by the stress relaxation effect.

4.3 FE simulation of stress and strain distribution inside the TRIP steel

Since the neck geometry governed the distribution of the stress state in the analytical approaches [39,40], a geometric agreement was assumed to result in the same stress states inside the neck. However, the stress and strain distributions for each state differed according to the hardening laws, as explained in this section.

The stress and strain distributions inside the TRIP steel specimens at $\rho = 0.86$ were simulated as shown in Figure 18. Clearly, the original Swift hardening law applied in Case 3 resulted in a weaker localization of the state values for hydrostatic stress, stress-triaxiality, and equivalent plastic strain at the neck (Figure 18 (a-1, b-1, and c-1), respectively) compared with the other cases. The switching of the n value in Case 4 caused more stress and strain localization at the neck, as shown in Figure 18(a-2, b-2, and c-2). Case 5 ($f_{sat} = \infty$) presented more x-directional, diffused, and high hydrostatic stress regions compared with the other hardening laws at the neck Figure 18(a-3). Note that the areas of high equivalent plastic strain were similar for Cases 3, 4, and 5 Figure 18(c-1, c-2, and c-3). Imposing f_{sat} in Cases 6 and 7 increased the stress and strain localization in the neck. This was most remarkable in Case 7 ($f_{sat} = 0.2$), in which the three state values at the necked center were the largest of all five FE simulations, as shown in Figure 18(a-5, b-5, and c-5).

The above results suggest that the stress-triaxiality hardening suppressed deformation localization without changing the neck geometry or deviating from the σ_t–ρ curve, which indicates that the spatial maximum stress triaxiality was at the same level as when using the original Swift hardening law in Case 3. Furthermore, the deactivation of the stress-triaxiality hardening increased the stress and strain localization compared to the case without deactivation. It is notable that Case 7 ($f_{sat} = 0.2$) produced the highest hydrostatic stress and stress triaxiality at the neck center. The saturation of f caused a sudden decrease in the hardening rate by $n_2 = 0.02$. This very small n_2-induced, localized deformation was connected to the higher hydrostatic stress and stress triaxiality.

Since the TRIP effect has been observed to suppress stress and strain localization during tensile deformation [12], stress triaxiality was also considered small at fracture strain. However, as clarified in this study, the combination of the TRIP effect and its deactivation was observed to accelerate the stress-triaxiality development at the neck. Thus, in spite of concerns related to over-simplification, the $M_0 f$ term proposed in this study to describe the stress-triaxiality hardening can be regarded reasonable.

4.4 Microstructural analysis of stress-triaxiality hardening and damage effect

In this study, the XRD peaks of the austenite lattice planes were observed to weaken or diminish in the post-neck strain region, as exemplified in Figure 8. The textured crystal orientation of the retained austenite (see Figure 1(b)) possibly caused these peak dissipations. Thus, instead of using the XRD evaluation of austenite volume fraction, the SEM and EBSD images close to the fracture surface of the tensile specimen were employed to investigate the microstructure as presented in Figure 19.

Figure 19(a) presents the remaining retained austenite around the fracture surface, which shows evidence of stress-triaxiality hardening in the post-neck strain region. However, we could not validate the

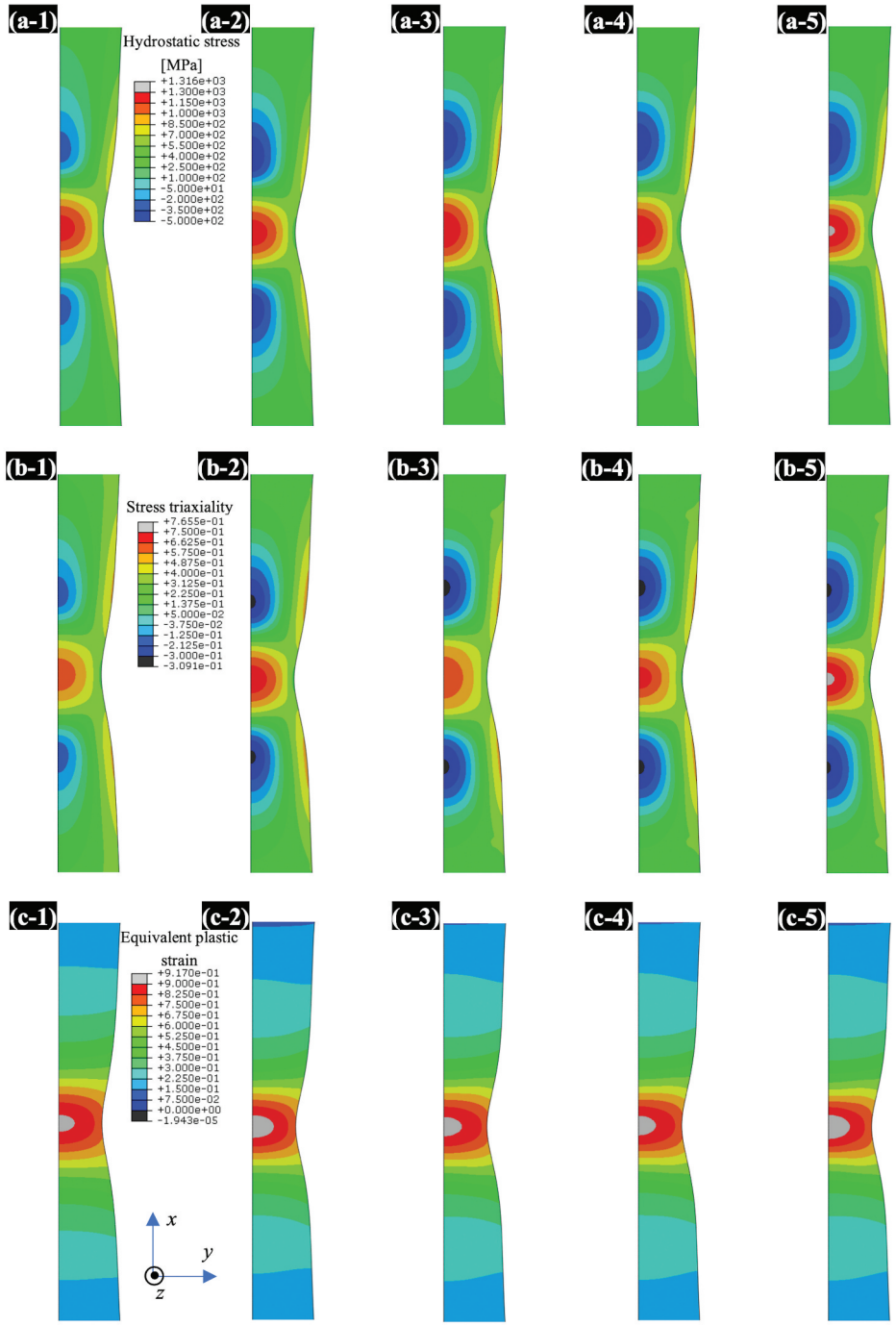

Figure 18. Contour maps of the simulated state values of the TRIP steel at a $\rho = 0.86$. The letters a, b, and c denote the hydrostatic stress, stress triaxiality, and equivalent plastic strain, respectively. The numbers 1–5 denote Cases 3–7, respectively.

TRIP effect saturation, $f_{sat} = 0.2$, using the microstructure due to the insufficient measurement of the volume fraction history of the austenite. Instead, the TRIP effect saturation was suggested based on a comparison between the FE simulations and the XRD stress measurements, but detailed analyses are required to improve the stress distribution inside the specimen. Indeed, the stress-triaxiality-induced austenite transformation disturbs the stress states inside the specimen, which accelerate or suppress further transformation due to material deformation. This analysis will therefore be a topic of future research.

Additionally, note that Figure 19(b) indicates the presence of micro voids around the fracture surface. The void area fractions in the SEM images were evaluated to be approximately 0.84 % of 5,372 μm^2. This micro void observation implies the effect of damage on the σ_t–ρ curves and stress/strain distribution inside the specimen, but this effect is small. In an elasto-plastic analysis, the damage D decreases the true stress σ_t as follows [41]:

$$\sigma_t = (1 - D)\sigma_t^* \tag{17}$$

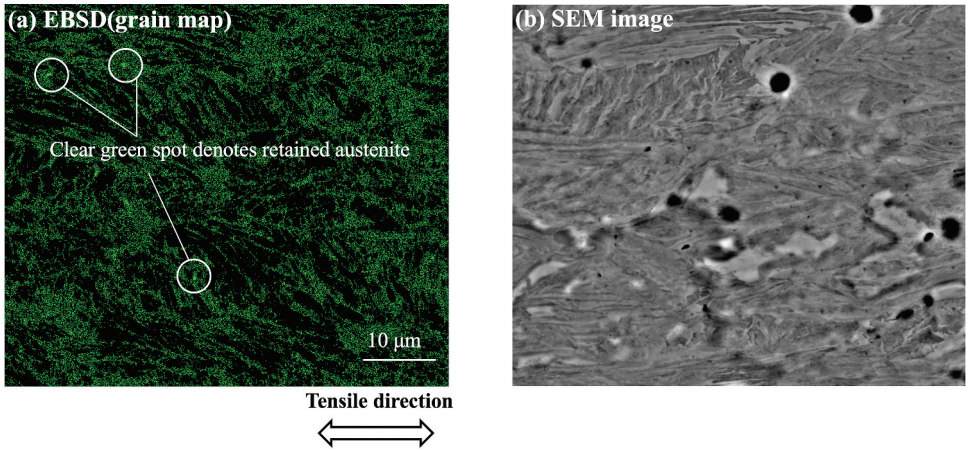

Figure 19. Microstructure around the fractured surface of the tensioned TRIP steel observed via (a) EBSD image obtained with a 0.04 μm step and (b) SEM image.

where σ_t^* denotes true stress in the matrix. Assuming $D \approx 0.0084$ based on the void area fraction around the fracture surface, the material damage possibly decreased by at most 15 MPa from σ_t^* in the measured σ_t range for the TRIP steel. Therefore, stress-triaxiality hardening can be regarded to mainly affect the deformation behavior.

5. Conclusion

We analyzed the stress-triaxiality hardening of advanced TRIP steel in the post-necking strain region. The post-necking strain hardening behavior of conventional DP steel was also analyzed to provide a reference. Small, round-bar tensile tests with specimen shape monitoring were used to evaluate the true stress vs. cross-sectional reduction ratio curves in the post-necking strain region up to fracture. In-situ synchrotron XRD measurements were also conducted during these tests to evaluate the stress inside the specimen necks. These measurements were then compared with the FE simulations conducted using simplified hardening laws. The results can be summarized as follows:

(1) The FE simulation employing the original Swift law agreed well with the true stress vs. cross-sectional reduction ratio curve, neck geometry, and stress distribution in the post-necking strain region for the DP steel.
(2) In contrast to the DP steel, the hardening rate of the TRIP steel showed a sudden decrease at the uniform elongation limit strain. The FE simulations employing n value decreased from 0.28 to 0.02 and including stress-triaxiality hardening terms successfully reproduced this hardening behavior up to the fracture.
(3) The FE simulation including stress-triaxiality hardening and its saturation presented the closest values to the XRD measurements obtained during the tensile tests for the TRIP steel. This simulation also agreed well with the measurements obtained in the tensile direction away from the neck center. A microstructural analysis of the retained austenite at the neck supported this result.
(4) The FE simulations revealed that a combination of the TRIP effect and its deactivation accelerates the localized deformation at the specimen neck under tensile loading. A smaller n value and larger stress-triaxiality hardening effect provided an FE simulation result closer to the actual stress and strain distribution observed inside the tensile specimen.

Acknowledgements

We gratefully acknowledge the work of past and present members of Tottori University laboratory: Tomoya Yoshioka, Reon Ando, Iori Sanou, Takahiro Fujii, Kouta Nakagiri, Maho Soko, and Yusuke Nakagawa.

Disclosure statement

No potential conflict of interest was reported by the authors.

Funding

This work was performed under the GIMRT Program of the Institute for Materials Research, Tohoku University (Proposal No. 18K0024, 19K0037, 20K0008) and was supported by the Japan Society for the Promotion of Science (KAKENHI, JP 20H02484). The synchrotron radiation experiments were performed at BL28B2 at SPring-8 with the approval of the Japan Synchrotron Radiation Research Institute (JASRI) (Proposal No. 2018B1318).

ORCID

Takashi Matsuno http://orcid.org/0000-0002-8530-6652

Tomohiko Hojo http://orcid.org/0000-0002-2558-4781
Ikumu Watanabe http://orcid.org/0000-0002-7693-1675

References

[1] Pednekar V, Khutorsky A, Lad S, et al. Third generation 980 class AHSS: a viable alternative to replace press-hardenable steels (PHS) in automotive rear rail applications. SAE Tech Paper. 2020;Article no. 2020-01-0534. DOI:10.4271/2020-01-0534.
[2] Khan AS, Baig M, Choi SH, et al Quasi-static and dynamic responses of advanced high strength steels: experiments and modeling. Int J Plast. 2012;30–31:1–17.
[3] Frommeyer G, Brüx U, Neumann P. Supra-ductile and high-strength manganese-TRIP/TWIP steels for high energy absorption purposes. ISIJ Int. 2003;43:438–446.
[4] Tomoda Y. Crystallographic characterization of steel microstructure using neutron diffraction. Sci Technol Adv Mater. 2020;20:1189–1206.
[5] Ushioda K. Advances in research on deformation and recrystallization for the development of high-functional steels. Sci Technol Adv Mater. 2020;21:29–42.
[6] Ohata M, Toyoda M. Damage concept for evaluating ductile cracking of steel structure subjected to large-scale cyclic straining. Sci Technol Adv Mater. 2004;5:241–249.
[7] Hance BM. Advanced high-strength steel (AHSS) performance level definitions and targets. SAE Int J Mater Manuf. 2018;11:505–516.
[8] Olson GB, Azrin M. Transformation behavior of TRIP steels. Metall Trans A. 1978;9:713–721.
[9] Olson GB, Cohen M. Stress-assisted isothermal martensitic transformation: application to TRIP steels. Metall Trans A. 1982;13:1907–1914.
[10] Stringfellow RG, Parks DM, Olson GB. A constitutive model for transformation plasticity accompanying strain-induced martensitic transformations in metastable austenitic steels. Acta Metall Mater. 1992;40:1703–1716.
[11] Tomita Y, Iwamoto T. Computational prediction of deformation behavior of TRIP steels under cyclic loading. Int J Mech Sci. 2001;43:2017–2034.
[12] Papatriantafillou I, Agoras M, Aravas N, et al. Constitutive modeling and finite element methods for TRIP steels. Comp Meth Appl Mech Eng. 2006;195:5094–5114. .
[13] Kohar CP, Cherkaoui M, El Kadiri H, et al Numerical modeling of TRIP steel in axial crashworthiness. Int J Plast. 2016;84:224–254.
[14] Kubler RF, Berveiller M, Buessler P. Semi phenomenological modelling of the behavior of TRIP steels. Int J Plast. 2011;27:299–327.
[15] Choi KS, Liu WN, Sun X, et al Microstructure-based constitutive modeling of TRIP steel: prediction of ductility and failure modes under different loading conditions. Acta Materialia. 2009;57:2592–2604.
[16] Pham QT, Lee BH, Park KC, et al Influence of the post-necking prediction of hardening law on the theoretical forming limit curve of aluminium sheets. Int J Mech Sci. 2018;140:521–536.
[17] Tang B, Wu F, Wang Q, et al Damage prediction of hot stamped boron steel 22MnB5 with a microscopic motivated ductile fracture criterion: experiment and simulation. Int J Mech Sci. 2020;169:105302.
[18] Kim JH, Serpantié A, Barlat F, et al. Characterization of the post-necking strain hardening behavior using the virtual fields method. Int J Sol Struct. 2013;50:3829–3842. .
[19] Scales M, Chen K, Kyriakides S. Material response, localization, and failure of an aluminum alloy under combined shear and tension: part I experiments. Int J Plast. 2019;120:340–360.
[20] Roth CC, Morgeneyer TF, Cheng Y, et al Ductile damage mechanism under shear-dominated loading: in-situ tomography experiments on dual phase steel and localization analysis. Int J Plast. 2018;109:169–192.
[21] Coppieters S, Kuwabara T. Identification of post-necking hardening phenomena in ductile sheet metal. Exp Mech. 2014;54:1355–1371.
[22] Coppieters S, Cooreman S, Sol H, et al Identification of the post-necking hardening behaviour of sheet metal by comparison of the internal and external work in the necking zone. J Mater Process Technol. 2011;211:545–552.
[23] Marth S, Hå H, Oldenburg M, et al Post necking characterisation for sheet metal materials using full field measurement. J Mater Process Technol. 2016;238:315–324.
[24] Joo G, Huh H. Rate-dependent isotropic-kinematic hardening model in tension-compression of TRIP and TWIP steel sheets. Int J Mech Sci. 2018;146:432–444.
[25] Mirone G. A new model for the elastoplastic characterization and the stress–strain determination on the necking section of a tensile specimen. Int J Sol Struct. 2004;41:3545–3564.
[26] Murata M, Yoshida Y, Nishiwaki T. Stress correction method for flow stress identification by tensile test using notched round bar. J Mater Process Technol. 2018;251:65–72.
[27] Sugimoto K, Tsunezawa M, Hojo T, et al. Ductility of 0.1-0.6 C-1.5 Si-1.5 Mn ultra high-strength TRIP-aided sheet steels with bainitic ferrite matrix. ISIJ Int. 2004;44:1608–1614. 10.2355/isijinternational.44.1608
[28] Hojo T, Kikuchi R, Waki H, et al Effect of strain rate on the hydrogen embrittlement property of ultra high-strength low alloy TRIP-aided steel. ISIJ Int. 2018;58:751–759.
[29] Giessen BC, Gordon GE. X-ray diffraction: new high-speed technique based on X-ray spectrography. Science. 1968;159:973–975.
[30] Kröner E. Computation of the elastic constants of polycrystals from constants of single crystals. Z Phys. 1958;151:504–518.
[31] Shibano J, Shobu T, Suzuki K, et al Measurement of internal strain in materials using high energy white X-ray at SPring-8. Mater Sci Forum. 2008;571:267–270.
[32] Prasad K, Venkatesh B, Krishnaswamy H, et al On the interplay of friction and stress relaxation to improve stretch-flangeability of dual phase (DP600) steel. CIRP J Manuf Sci Technol. 2021;32:154–169.
[33] Matsuno T, Shoji H, Ohata M. Fracture strain measurement of steel sheets under high hydrostatic pressure. Procedia Manuf. 2018;15:869–876.
[34] Yang SY, Tong W. A finite element analysis of a tapered flat sheet tensile specimen. Exp Mech. 2009;49:317–330.
[35] Shirakami S, Tsunemi Y, Yoshida T, et al Work-hardening behaviour of sheet steels in large strain

regions and its simple approximation. J Phys Conf Ser. 2018;1063:012107.
[36] Swift HW. Plastic instability under plane stress. J Mech Phys Sol. 1952;1:1–18.
[37] Ennis BL, Jimenez-Melero E, Atzema EH, et al Metastable austenite driven work-hardening behaviour in a TRIP-assisted dual phase steel. Int J Plast. 2017;88:126–139.
[38] Hu XH, Sun X, Hector LG Jr, et al Individual phase constitutive properties of a TRIP-assisted QP980 steel from a combined synchrotron X-ray diffraction and crystal plasticity approach. Acta Materialia. 2017;132:230–244.
[39] Davidenkov NN, Spiridonova NI. Analysis of the state of stress in the neck of a tensile test specimen. Proc ASTM. 1946;46:1147–1158.
[40] Bridgman PW. Studies in large plastic flow and fracture. New York (NY): McGraw-Hill; 1952.
[41] Lemaitre J. A continuous damage mechanics model for ductile fracture. J Eng Mater Technol. 1985;107:83–89.